Chemical Science

ROYAL SOCIETY OF CHEMISTRY

EDGE ARTICLE

View Article Online
View Journal | View Issue

Cite this: *Chem. Sci.*, 2025, **16**, 16121

All publication charges for this article have been paid for by the Royal Society of Chemistry

Hydrogen/solvent-free plastic valorization *via* loosely coordinated ruthenium sites steering selective aromatization

Fan Mo,[ab] Qixing Zhou, *[b] Pengfei Wang,[b] Weitao Liu, [b] Chuan Yin,[b] Zelin Hou,[b] Wendan Xue,[b] Qi Wang,[b] Jianling Wang,[b] Tong Zheng,[b] Zongxin Tao[b] and Xiang Li[b]

The development of hydrogen- and solvent-free catalytic systems for plastic valorization requires precise control over metal speciation to enhance both catalytic efficiency and selectivity. Ru atomic clusters (ACs) on HZSM-5 zeolite show a turnover frequency of 52.71 mg_{LDPE} mg_{Ru}^{-1} h^{-1} in low-density polyethylene (LDPE) conversion, a fivefold increase compared to traditional nanoparticles (NPs) at 10.63 mg_{LDPE} mg_{Ru}^{-1} h^{-1}. This improved catalytic performance is further evident in cyclohexane dehydroaromatization, where atomic-scale Ru sites exhibit a 17.8-fold activity increase (544.34 *vs.* 30.48 μM mg_{Ru}^{-1} h^{-1}), linking subnanometric structures to reaction pathway selectivity. Mechanistic analysis highlights two key effects: (1) optimized interactions between isolated Ru sites and intermediates lower dehydrogenation barriers, and (2) reduced cyclization energy barriers compared to NPs. Process optimization leads to 87% LDPE conversion with 69% aromatic selectivity, maintaining 70% efficiency across various polyolefins (including high-density PE and ultra-high-molecular-weight PE) and polystyrene. A techno-economic analysis shows the potential of AC catalysts, predicting a net present value of 1.78 million over five years, compared to an annual loss of 8.17 million for NPs. This study demonstrates the critical role of metal dispersion and acid–metal balance, forming the basis for a sustainable plastic-to-aromatics process with strong economic viability.

Received 25th June 2025
Accepted 24th July 2025

DOI: 10.1039/d5sc04662a

rsc.li/chemical-science

1 Introduction

Over the past 70 years, global production of synthetic, petroleum-based plastics has surged from under 2 million tonnes in 1950 to 430 million tonnes in 2023, with projections indicating it will double again within the next 20 years, resulting in potential environmental accumulation and negative ecological impacts.[1–4] Current recycling methods (*e.g.*, landfills or incineration) are economically inefficient and lack sustainability. Recently, hydrogen- and solvent-free upcycling methods (*i.e.*, thermodynamically feasible recovery by coupling exothermic hydrogenolysis with endothermic aromatization) have emerged as a promising research direction.[1,5] However, these approaches necessitate the optimization of cost, efficiency, and selectivity before they can be feasibly implemented.

Noble metal-based catalysts are integral to optimizing the efficiency and selectivity of plastic upcycling processes, while concurrently mitigating the formation of harmful byproducts. However, their widespread application is constrained by challenges such as high cost, low catalytic activity, and insufficiently tunable selectivity.[6] Several strategies, such as entropy confinement,[7] construction of strong metal–support interaction,[8] regulation of particle size,[9,10] *etc.*, have been developed for strengthening plastic hydrogenolysis. Among them, controlling the atomic assembly degree—specifically, optimizing the ensemble requirements for particular reactions—can substantially minimize expenditure. In ammonia synthesis, Ru NPs larger than 1–2 nm were required,[11] whereas the Fischer–Tropsch synthesis favored Co NPs exceeding 6 nm.[12] For the oxidation of methane to methanol, Cu dimers or cluster species within zeolite frameworks (such as ZSM-5, MOR, SSZ-13, SAPO-34, *etc.*) were essential for O_2 dissociation, as a mononuclear metal center without functional ligands was insufficient for completing the transformation.[13,14] Additionally, the Pt/Al_2O_3 catalyst demonstrated a significant activity enhancement for ethylene hydrogenation when utilizing Pt atomic clusters (ACs) of approximately 0.6 nm, compared to Pt nanoparticles (NPs) larger than 1 nm. However, a further reduction in size resulted in decreased activity, indicating that Pt ACs around 0.6 nm provided the optimal ensemble requirement for the hydrogenation of C=C bonds.[15] Nevertheless, there is a paucity of

[a]*SEP Key Laboratory of Eco-industry, School of Resources and Civil Engineering, Northeastern University, 11 Wenhua Road, Heping District, Shenyang, 110819, P.R. China*

[b]*Key Laboratory of Pollution Processes and Environmental Criteria (Ministry of Education)/Tianjin Key Laboratory of Environmental Remediation and Pollution Control, Carbon Neutrality Interdisciplinary Science Center, College of Environmental Science and Engineering, Nankai University, Tianjin 300350, China. E-mail: zhouqx@nankai.edu.cn*

studies examining the impact of assembly degree on hydrogen- and solvent-free plastics' upcycling processes.

Typically, hydrogen- and solvent-free plastic upcycling involves a range of reactions, including β-scission, hydrogenolysis, dehydrogenation, hydrogen migration, dehydro-aromatization, and re-hydrogenation of aromatics, among others. A recent study mainly concentrated on the conversion of waste plastics into alkanes and alkenes;[16] however, the focus on aromatic products remains shrouded in ambiguity. Aromatic hydrocarbons are instrumental in the synthesis of advanced polymers, the formulation of sophisticated solvents, and the development of complex pharmaceuticals, among various other high-value applications. Adjusting the dehydrogenation depth to facilitate benzene ring formation while preventing coke deposition, as well as suppressing β-scission, hydrogenolysis, and re-hydrogenation of the benzene ring, is a crucial method for achieving substantial yields of aromatics. AC active sites possess the following advantages in the dehydrogenation reaction:[17] (i) the highly exposed active sites on ACs, characterized by coordination unsaturation, markedly optimize the adsorption of reactants and intermediates, thereby facilitating efficient C–H activation. (ii) The optimal electronic properties of the atomic surface promote the desorption of products, effectively reducing over-dehydrogenation and minimizing coke formation. However, optimizing the characteristics of active sites to achieve superior aromatics yields—by precisely tuning the dehydrogenation depth and inhibiting the side reactions in complex chain reactions—remains a challenging and intricate issue.

In this study, a strategy leveraging the discretization of active sites was implemented in a hydrogen- and solvent-free system to directly convert common plastics into valuable hydrocarbon products, particularly aromatics. Ru ACs with isolated atomic sites, in contrast to Ru NPs exhibiting continuous lattice fringes, significantly enhanced both the conversion rate and aromatic selectivity. This improvement can be attributed to minimized side reactions, including β-scission, hydrogenolysis, and the re-hydrogenation of aromatics, coupled with enhanced dehydrogenation and dehydro-aromatization efficiencies. Consequently, the thermal upcycling process utilizing Ru ACs markedly improved economic benefits. Specifically, the turnover frequency (TOF) increased from 10.52 $mg_{LDPE}\ mg_{Ru}^{-1}\ h^{-1}$ for Ru NP-loaded HZSM-5-300H to 52.40 $mg_{LDPE}\ mg_{Ru}^{-1}\ h^{-1}$ for Ru AC-loaded HZSM-5-300H. Moreover, the optimized catalyst reduced the metal loading from 1.5 wt% for Pt/γ-Al_2O_3 and approximately 6.89 wt% for Ru/HZSM-5 to just 0.5 wt% in Ru AC-loaded HZSM-5-300H and enhanced TOFs from 1.31 and 4.04 to 52.71 $mg_{PE}\ mg_{Ru}^{-1}\ h^{-1}$,[1,5] significantly lowering capital input and enhancing economic efficiency. The industrial simulation results revealed that the 0.5R/300H configuration demonstrated significantly enhanced economic feasibility compared to the 2R/300H, as evidenced by the superior average return on investment (ROI) of 30.06%, a shorter payback period (PBP) of 2.66 years, and an internal rate of return (IRR) of 16%, all without depreciation. Additionally, the net present value (NPV) was positive at $1 778 301.25 within 5 years, again without depreciation. In stark contrast, the 2R/300H configuration showed a negative annual gross profit of $-8 169 496.5, also without depreciation.

2 Results and discussion

2.1 Deciphering the interdependence of upcycling performance and active site morphological features

2.1.1 Deciphering the interdependence of upcycling performance and metal incorporation amount. The series *X*R/*Y*H (where $X = 0, 0.2, 0.35, 0.5, 0.75, 1, 2, 3$; $Y = 300, 150, 75$) was constructed using a combination of impregnation and reductive calcination methods (Fig. S1). The upcycling activity was initially investigated in relation to metal loading, with a focus on the attributes of the particles. The low-density polyethylene (LDPE) thermal upcycling was conducted in *X*R/300H/solvent/H_2-free systems ($X = 0, 0.2, 0.35, 0.5, 0.75, 1, 2, 3$). The 0.5R/300H exhibited the highest upcycling rate of 62.93% (Fig. 1a and S2), with aromatics selectivity up to 70.43% (*i.e.*, carbon numbers ranging from 7 to 16 and peaking at 8, Fig. 1b and c). By contrast, other *X*R/300H systems delivered inferior plastic conversion and aromatics selectivity, with conversion rates/selectivity of 35.52/29.13%, 41.61/48.43%, 47.88/49.87%, 53.54/59.94%, 51.66/43.65%, 49.41/48.07% (*i.e.*, carbon numbers range from 7 to 16, peaking at 8, with a higher proportion of alkanes and a lower proportion of aromatics generated, Fig. 1b and c), and 50.37/51.10% for 300H, 0.2R/300H, 0.35R/300H, 0.75R/300H, 1R/300H, 2R/300H, and 3R/300H, respectively, underscoring the superiority of low-loaded Ru species compared to those with higher loading. Therefore, 0.5 and 2 wt% were chosen as the typical representative mass fraction. The NMR analysis of liquid products gave a similar conclusion as well, showing that more aromatics-related H can be detected in 0.5R/300H ($H_{Ar+Ph}/H_{Total} = 0.5$) compared to those in 2R/300H ($H_{Ar+Ph}/H_{Total} = 0.42$) (Fig. S3 and S4). Note that minimal changes in conversion rate and aromatics selectivity were observed with Ru loadings ranging from 1 wt% to 3 wt%, attributed to the structure-insensitivity of the metal NPs (*i.e.*, continuous lattice fringe catalysis), as the structure sensitivity typically emerged when the metal size was reduced to sub-nanometer or atomic scales.[18] It can be speculated that the Ru species may favorably substitute the Brønsted acid sites (BAS) to preclude the side reaction (*e.g.*, β scission-facilitated C–C cleavage) and intrinsically enable the synergistic action with BAS, evidenced by the inferior conversion rate and aromatics selectivity over pure HZSM-5-300H.[19]

Furthermore, the upcycling capacity of other common supports (*e.g.*, Hβ and Al_2O_3) and metal (*e.g.*, Ir) were determined (Fig. 1d and S5). Hβ-zeolite-supported Ru species, metal Ir-loaded HZSM-5-300H, and Al_2O_3-supported Ru species all exhibited a dependence on metal loading, with lower incorporation amounts showing enhanced upcycling activity and aromatics selectivity relative to higher loadings. Among these, Ru ACs supported on HZSM-5-300H demonstrated the highest aromatic yield and overall conversion efficiency under identical loading conditions (*i.e.*, nominal 0.5 wt%). This finding highlighted the broader applicability of this principle across different support materials (including HZSM-5-150H and

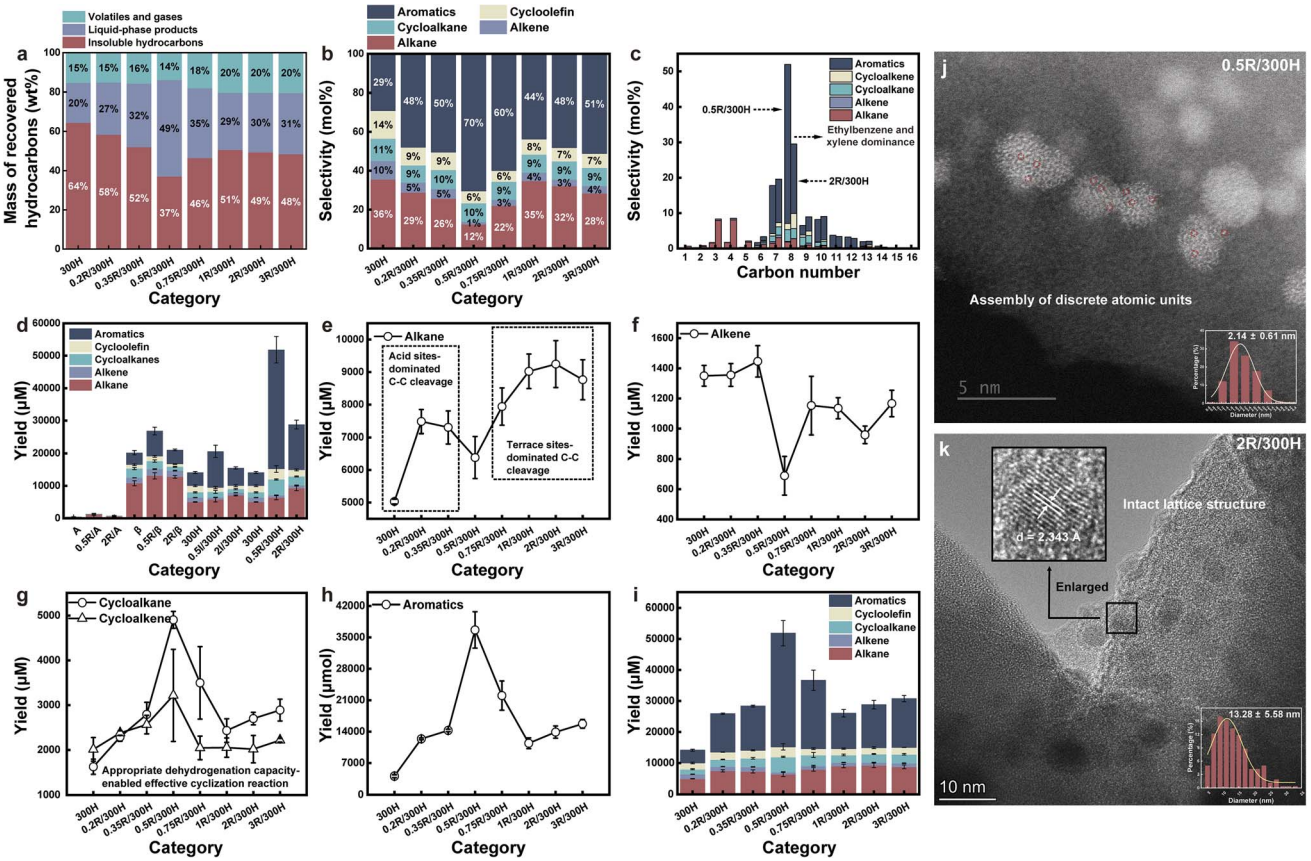

Fig. 1 The relationship between upcycling performance and active site features. (a) Selectivity of volatiles/gases, liquid-phase products, and insoluble hydrocarbons in a series of *X*R/300H/LDPE/H_2-free/solvent-free systems. (b) Selectivity of alkanes, alkenes, cycloalkanes, cycloolefins, and aromatic products in a series of *X*R/300H/LDPE/H_2-free/solvent-free systems. (c) Detailed hydrocarbon selectivity of alkanes, alkenes, cycloalkanes, cycloolefins, and aromatics with varying carbon numbers. (d) Determined molar quantities of products from LDPE upcycling mediated by metal Ru-loaded Al_2O_3 (A), Hβ (β), 300H, and metal Ir-loaded 300H. Total molar yields of (e) alkane, (f) alkene, (g) cycloalkane and cycloalkene, and (h) aromatics in a series of *X*R/300H/LDPE/H_2-free/solvent-free systems. (i) Molar yields of products in a series of *X*R/300H/LDPE/H_2-free/solvent-free systems. (j) Atomic-resolved HAADF-STEM images of 0.5R/300H, with red circles indicating the atomic sites. (k) TEM images of 2R/300H. The particle size statistics were derived from the analysis of multiple images (particle count greater than 200), based on the long axes of irregular shapes.

HZSM-5-75H, refer to Section 2.4). Accordingly, HZSM-5-300H and metal Ru species were selected as the representative support and active sites.

The relationship between the yields of partial products—namely alkanes, alkenes, cycloalkanes, cycloolefins, and aromatics—and the amounts of metal loading was investigated. It was apparent that both low- and high-Ru-loaded HZSM-5-300H catalysts significantly enhanced alkane/alkene formation compared to the 0.5R/300H catalyst (Fig. 1e). This improvement was attributed to the greater abundance of moderate acid sites (*i.e.*, driving β-scission) in the 0.2R/300H and 0.35R/300H samples and the more abundant terrace sites (*i.e.*, facilitating hydrogenolysis) in the 0.75-3R/300H samples relative to 0.5R/300H (Fig. S6). These factors collectively facilitated more effective C–C cleavage processes, resulting in an increased yield of alkanes/alkene.

BAS sites facilitate the conversion of C=C bonds into carbenium ions but do not mediate the dehydrogenation of polymer chains to generate C=C bonds. When an excess of C=C bonds is converted into carbenium ions without a commensurate increase in C=C bonds, there is an inadequate supply of C=C bonds to interact with carbenium ions. This leads to a higher propensity for β-scission rather than cyclization.[5,17] Therefore, it can be concluded that the 0.5R/300H catalyst exhibited superior performance in both dehydrogenation (by optimizing the C=C to carbenium ion ratio, thereby promoting cyclization and inhibiting β-scission) and aromatization (through effective dehydro-aromatization that greatly enhanced aromatics formation), as evidenced by its minimal alkane/alkene yield and maximal cyclohexane/cycloolefin/aromatics production (Fig. 1e–i). To sum up, the product distribution pattern highlighted the higher dehydro-aromatization and hydrogenolysis capacity for 0.5R/300H and 2R/300H, respectively.

The adsorption behavior of the polymer can largely influence the product selectivity. Typically, the hydrogenolysis is affected by the hydrocarbon adsorption to the catalyst and the probability scales linearly with the molecular weight.[20] Simultaneously, the adsorption energy is often inversely proportional to the dispersity. Typically, the higher the dispersion, the lower the

adsorption energy, and *vice versa*.[19] Therefore, it can be speculated that 2R/300H more energetically adsorbed the polymer compared to 0.5R/300H, leading to increased C–C cleavage, which was also closely related to H* coverage. Besides, the dehydro-aromatization was associated closely with the atomic dispersity as well, which was associated with the atomic assembly degree. Therefore, an initial investigation into the dispersity of active sites was conducted through microscopic characterization.

2.1.2 Deciphering the morphological features of active sites. To investigate the characteristics of active sites, the atomic-scale structure of the Ru species-loaded HZSM-5-300H was determined by aberration-corrected scanning transmission electron microscopy (AC-STEM). The 0.5R/300H showed predominant aggregates of isolated Ru atoms without an intact crystal face being identified (Fig. 1j). With the increase of Ru loading from 0.5 wt% to 2 wt%, a clear lattice fringe emerged, and the geometry of Ru ACs evolved from ensembles with several incompact single atoms (SAs) to NPs featuring clear crystalline structures (Fig. 1k). The average size of the Ru assembly gradually increased from around 2.14 ± 0.61 nm to 13.28 ± 0.58 nm (Fig. 1j and k). Note that isolated Ru atoms cannot be identified, resulting in the classification of pure ACs or NP-mediated thermo-upcycling in this study, which was consistent with the presence of bridge-bound CO signals in CO-diffuse reflectance infrared Fourier transform spectroscopy (DRIFTS), while linear-bound CO signals were absent (Fig. 2h).

The increased thermo-upcycling activity of ACs may thus be linked to their more diverse and accessible active sites compared to the more ordered and constrained active sites on NP counterparts. ACs, typically consisting of a smaller number of atoms, exhibit a higher surface atom ratio and increased surface energy, leading to more active sites being established. In contrast, NPs often have well-defined crystal facets with limited active sites, restricting their thermo-catalytic performance. For example, the proportion of corner atoms diminished by nearly a factor of three with only a marginal increase in cluster size from 1.6 nm to 2.2 nm.[19] EDX analysis further confirmed the existence of Ru NPs (Fig. S7 and S8). The atomic Ru sites (*i.e.*, 0.2R/300H) failed to effectively mediate the plastic conversion (41.61/48.43%, lowest conversion rate across the Ru-loaded HZSM-5-300H). It can be concluded that the over-dispersed surface-bound Ru atoms were unlikely to accommodate C–C bonds and H adatoms concurrently (Fig. S9), and will consequently be omitted from the subsequent discussion.[21] These results verified that the Ru NPs with a continuous lattice plane and Ru ACs with discrete atomic sites would favor hydrogenolysis and dehydro-aromatization, respectively. The more detailed structural and electronic properties of Ru ACs and NPs were further investigated using various characterization techniques.

2.2 Dissecting the structural and electronic characteristics of *X*Ru/300H

2.2.1 Unveiling the attributes of acidic sites and pore structures. The characteristics of acidic sites and pore structures were initially investigated. Fourier transform infrared spectroscopy using pyridine as a probe molecule (pyridine-FTIR) was used to monitor the acidic nature of the BAS and Lewis acid site (LAS). The clear 1598.63 and 1446.20 cm^{-1} feature bands were associated with the protonated pyridinium ion corresponding to BAS and coordinatively adsorbed pyridine on the LAS, respectively. It is worth noting that 2R/300H possessed higher acidity compared to 0.5R/300H, indicating that the differences in upcycling activity were not acid-dependent, likely relating to the intrinsic structure of the active sites (Fig. 2a and Table S3). The NH_3-TPD analysis showed similar results (Fig. 2b). 2R/300H exhibited a higher intensity of moderate acidity compared to 0.5R/300H (with similar weak/strong acidity), also suggesting that the enhanced polymer upcycling capacity was primarily dominated by particle characteristics (Fig. 1b). In addition, the Ru incorporation significantly enhanced the B and L acidity but decreased the medium-strength acidity, due to its drastic interaction with HZSM-5 or serving as an intrinsic acid center (*i.e.*, reductive solid-state ion-exchange process, Fig. 2a and b).[19] Besides, the correlation between LDPE upcycling and mass transport was excluded as well, due to the nearly similar pore characteristics (Fig. S13–19). Note that the weaker N_2 desorption capacity of 2R/300H compared to that of 0.5R/300H potentially indicated the stronger adsorption of small molecules on Ru NPs (Fig. S15), which was further verified by thermogravimetric analysis. The TGA showed that the 2R/300H retained more aromatics compared to 0.5R/300H during the LDPE upcycling, cyclohexane dehydrogenation, and *n*-hexadecane upcycling reactions (Fig. S20–S22), evidenced by the mass loss differences between 380 and 650 °C,[22] leading to the speculated correlation between inferior dehydro-aromatization to aromatics and excessive product adsorption on Ru NPs (poisoned active sites). For pure 300H, enhanced coke deposition was observed during cyclohexane dehydrogenation compared to 0.5R/300H, highlighting that the Ru incorporation can favorably optimize the acidity by neutralizing the original acid sites and construct superior metal–acid balance (*i.e.*, appropriate intermediate retention time on active sites).[19]

Typically, the narrow average pore size (*i.e.*, confined to 1–5 nm, Table S4) does not obstruct the ingress of polymer chains. In zeolites, the significant heats of adsorption—which increase linearly with carbon number for most zeolites and silicas—combined with the conformational entropy gains from chains adopting a more planar zig-zag configuration drive diffusion at high temperatures in microporous materials, in the absence of specific repulsive interactions. Consequently, the entropic benefits offset the enthalpic penalties arising from the partial confinement, resulting in the entry of the polymer chain, followed by Ru species-mediated thermal transformation.[23] Therefore, the intrinsic structural characteristics of Ru assembly were subsequently investigated.

2.2.2 Unveiling the structural and electronic attributes of Ru species. X-ray diffraction (XRD) was performed to reveal the crystal structure of 300H, 0.5R/300H, and 2R/300H (Fig. 2c). There was no sharp diffraction peak of Ru species (*i.e.* 2θ = 44.005, indexed to the (1 0 1) lattice plane, PDF #06-0663) in the

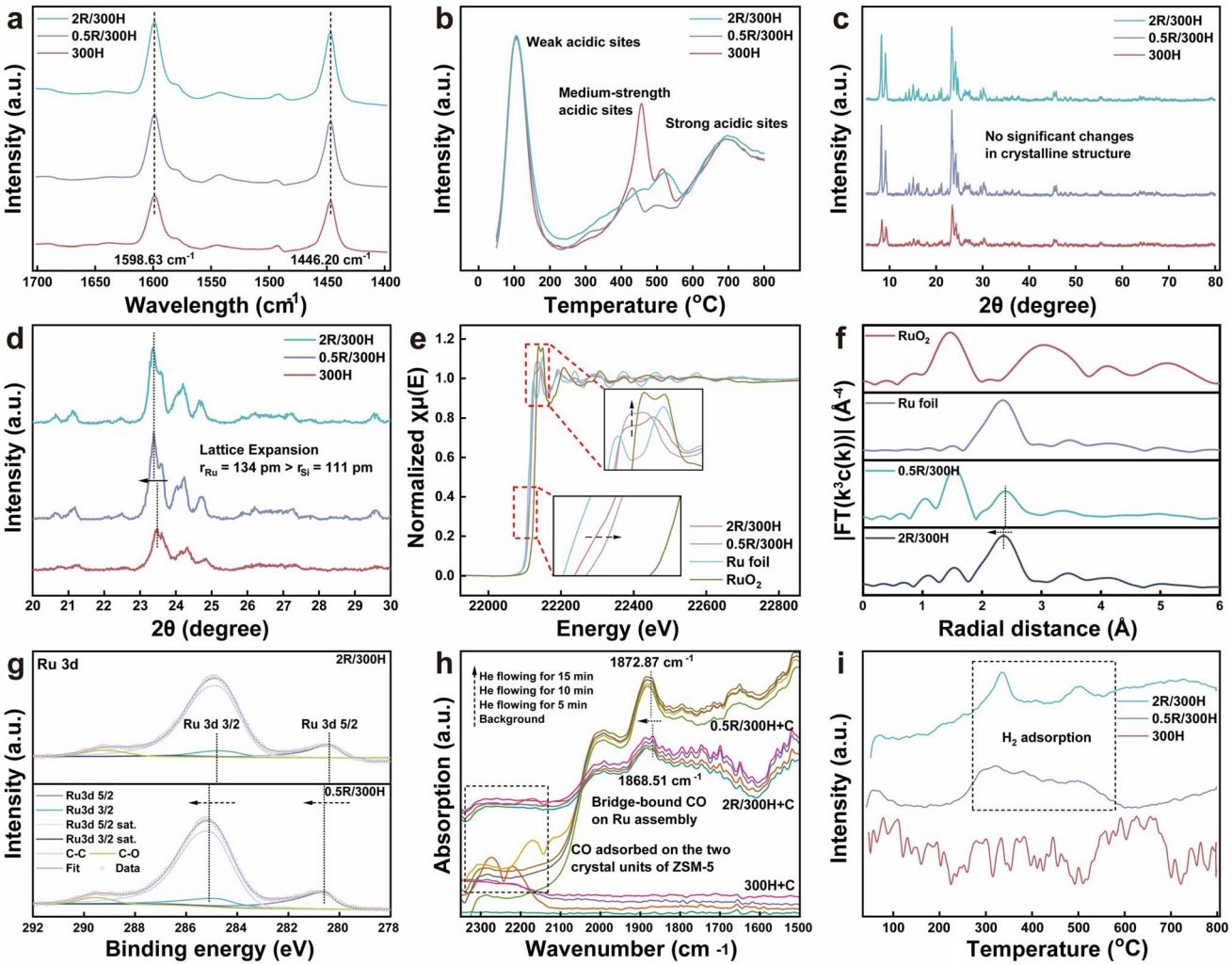

Fig. 2 Structural and electronic attributes of *X*Ru/300H. (a) FTIR measurements using pyridine as a probe molecule for 300H, 0.5R/300H, and 2R/300H collected at 200 °C. (b) NH_3-TPD analysis of 300H, 0.5R/300H, and 2R/300H. (c) XRD spectra of 300H, 0.5R/300H, and 2R/300H. (d) XRD spectra of 300H, 0.5R/300H, and 2R/300H, showing the enlarged area between 20° and 30°. (e) Ru-K edge XANES spectra for 0.5R/300H and 2R/300H. (f) Ru-K edge EXAFS spectra for 0.5R/300H and 2R/300H. (g) Ru 3d XPS analysis of 0.5R/300H and 2R/300H. (h) CO-DRIFTS spectra of 300H, 0.5R/300H, and 2R/300H within 2250–1500 cm^{-1} by flowing He gas at different times. C denotes cyclohexane. (i) H_2-TPR analysis of 300H, 0.5R/300H, and 2R/300H.

XRD patterns, indicating that Ru species were highly dispersed in the zeolite (*i.e.*, small particle size, 2.14 ± 0.61 and 13.28 ± 5.58 nm for 0.5R/300H and 2R/300H, respectively, Fig. 1j and k). Evident negative peak shifts were observed for 0.5R/300H and 2R/300H compared to 300H (Fig. 2d and S23), suggesting the occurrence of lattice expansion. Since the atomic radius of Ru (r_{Ru} = 134 pm) exceeds that of Si (r_{Si} = 111 pm), the observed changes in lattice parameters can be attributed to the intercalation of Ru and the modified structural properties of the supports upon interaction with the Ru assembly.

XAS was used to investigate the chemical state changes responsible for the differences in upcycling capacities (Fig. 1a, b, 2e and f). Firstly, the electronic state of Ru species was probed by XANES, showing the distribution of normalized white-line intensity and edge energy of 0.5R/300H and 2R/300H between those of Ru foil and RuO_2, indicating the existence of cationic Ru (Fig. 2e). As Ru loading decreased from 2 to 0.5 wt%, both the white-line intensity and the edge energy progressively increased, indicating that Ru become increasingly cationic with the reduction in particle size. These results can be supported by the XPS analysis (Fig. 2e), showing the shifts of binding energies of Ru 3d5/2 and Ru 3d3/2 from 280.4 and 284.8 eV on 2R/300H to 280.6 and 285.1 eV on 0.5R/300H, respectively, highlighting the close relationship between Ru valence state and particle size. No significant electron gain and loss can be observed for Si and O species, evidenced by the limited peak shift (Fig. S25 and S26). Meanwhile, increased electron gain was detected for Al species in 0.5R/300H compared to 2R/300H, indicating the occurrence of electron exchange between Ru species and acid sites (Fig. S27). These results highlighted the close relationship between particle structural characteristics and their electronic properties, due possibly to the varied atomic interaction force (*i.e.*, particle size, Fig. 1j and k) and metal–support interaction intensity.

The EXAFS results revealed that 0.5R/300H and 2R/300H predominantly exhibited metallic Ru–Ru scattering at approximately 2.7 Å, with a minor contribution from Ru–O scattering at around 2.0 Å (Fig. 2f and S28–32). As Ru loading decreased, Ru–Ru scattering weakened and N(Ru–Ru) decreased (from 3.42 ± 0.91 to 0.76 ± 0.36), undoubtedly indicating a reduction in Ru particle size (Table S5). Additionally, the increased Ru–Ru distance (from 2.68 ± 0.01 Å to 2.71 ± 0.01 Å) aligned with the formation of atomic assembly, due to the increased degree of disorder (the disappeared long-range order). These findings underscored significant structural changes in Ru particles, shifting from well-defined metallic NPs in 2R/300H to highly disordered species with no discernible structures beyond nearest neighbors in 0.5R/300H, which may account for the observed abrupt changes in polymer upcycling. Note that the Ru K-edge EXAFS feature of the reduced samples may entirely disappear if the incorporated Ru existed at the extra-framework position.[19] The clear EXAFS characteristics highlighted the strong interaction (*i.e.*, strong coordination pattern) between the Ru species and HZSM-5 framework.

CO-DRIFTS was further used to characterize the electronic and structural characteristics of surface Ru species (Fig. 2h). The bands at 2100–2200 cm^{-1} should be indexed to the vibration of CO adsorbed on the two crystal units of ZSM-5. The Ru incorporation induced the red shift of the CO adsorption peak on the crystal unit, highlighting the electron flow from 300H to the Ru assembly.[24] The adsorption shoulder peaks at 1871.07 and 1868.51 cm^{-1} are attributed to the bridged-bonded CO at two contiguous Ru atoms, indicating the formation of a Ru assembly, which accorded well with the AC-HAADF-STEM (Fig. 1j and k) results. Notably, a blue shift from 1868.51 cm^{-1} for 2R/300H to 1871.07 cm^{-1} for 0.5R/300H was observed, highlighting the decreased electronegativity (*i.e.*, increased valence state) of Ru ACs, decreasing the d-π electron feedback from Ru to the CO 2π* antibonding orbital.[19] In addition, the blue shift indicated a reduced interaction between Ru species and CO molecules, consistent with the emergence of relatively isolated Ru atoms that exhibited weaker interactions with CO.[19] The Ru ACs with a higher valence state (*i.e.*, possibly more cationic 2D rafts) would potentially deliver more active sites, low methane yield (Fig. S33) during polymer upcycling, and high reaction stability (*i.e.*, dominated 2D assembly of isolated Ru single atoms (SAs) and limited well-defined RuO_x aggregates for particle growth, Fig. 1j).[9] Note that the absorption bands at 3735 and 3591 cm^{-1} in DRIFTS are typically assigned to the external silanol group (Si–OH) and bridge OH group associated with BAS, respectively (Fig. S34). Their near absence in 0.5R/300H and 2R/300H suggested the substitution of Ru with BAS during reduction at 450 °C (*i.e.*, reductive solid-state ion-exchange process). The persistent bridge OH signal in 2R/300H potentially indicated a tendency towards agglomeration rather than complete ion exchange with BAS.[19]

The H_2-TPR technique was used to evaluate the H_2 binding capacity (Fig. 2i). It was observed that 0.5R/300H exhibited a more pronounced continuous absorption band for H_2 compared to 2R/300H, indicating a greater H_2 binding capacity for Ru ACs with more step sites relative to 2R/300H, which predominantly featured terrace sites. Additionally, superior H_2 spillover capacity can be expected for Ru ACs.[9] From an alternative perspective, the smaller size of the Ru assembly in 0.5R/300H resulted not only in increased exposure of Ru sites but also promoted a strong metal–support interaction (SMSI, Fig. S35) between Ru and 300H. These interactions are advantageous for the reduction of RuO_x species (*i.e.*, more favorable interaction with H_2).[24] Consequently, the interplay between the morphologies of Ru assemblies and their upcycling performance can be delineated, which was further elucidated through targeted probe experiments.

The techno-economic analysis (TEA) showed that the 0.5R/300H configuration outperformed the 2R/300H configuration in economic terms (Tables SE1–SE8 and Fig. SE1). Specifically, the ROI, PBP, IRR, and NPV for the 0.5R/300H configuration were 30.06%, 2.66 years, 16%, and \$1 778 301.25, respectively, without depreciation. In contrast, the 2R/300H configuration showed negative economic viability, with a negative annual gross profit of -\$-8 169 496.5, without depreciation, mainly due to inferior annual sales revenue (*i.e.*, low product yield) and more Ru cost input. Therefore, it can be concluded that using Ru ACs with isolated sites in HZSM-5 catalysts offers significantly better economic viability compared to using NPs with lattice plane.

2.3 An in-depth exploration of the mechanisms involved in the polymer upcycling

2.3.1 An in-depth exploration of the mechanisms involved in the polymer upcycling: probing reactions. Plastic thermal recycling primarily involves the cycling and competition of reactions such as β-scission, hydrogenolysis, dehydrogenation, aromatization, and hydrogenation, which were subtly investigated in the following section. Hexadecane was used as a substrate to evaluate the efficacy of the system in converting medium-chain alkanes (Fig. 3a). The results exhibited a significant reduction in aromatics selectivity (decreasing from 70.43% to 21% in the 0.5R/300H group, Fig. 1b), thereby reinforcing the rationale for using polymers as reactants to preferentially produce aromatics. Additionally, these findings indicated that long-chain alkanes are the primary contributors to the aromatization process, as the upcycling of hexadecane was predominantly dictated by the cleavage pathway rather than the aromatization pathway (*i.e.*, maximum selectivity of alkanes and alkenes relative to other products). Besides, the more ready aromatization and conversion capacities for Ru ACs compared to those for Ru NPs were verified, even with a medium-chain alkane reactant, showing higher aromatics selectivity (*i.e.*, 21% *vs.* 14% for 0.5R/300H and 2R/300H, respectively) and overall yield (*i.e.*, 81 473.05 *vs.* 48 774.55 μM for 0.5R/300H and 2R/300H, respectively, Fig. S36).

The hexadecane of medium length was selected as the model substrate to determine the hydrogenolysis capacity of 0.5R/300H and 2R/300H. More short-chain gaseous hydrocarbons (C1–C6) were formed in the 2R/300H/hexadecane/H_2 (*i.e.*, 21 937.44 μM) system compared to those in the 0.5R/300H/hexadecane/H_2 system (*i.e.*, 13 544.46 μM) (Fig. 3b, S39, and S40),

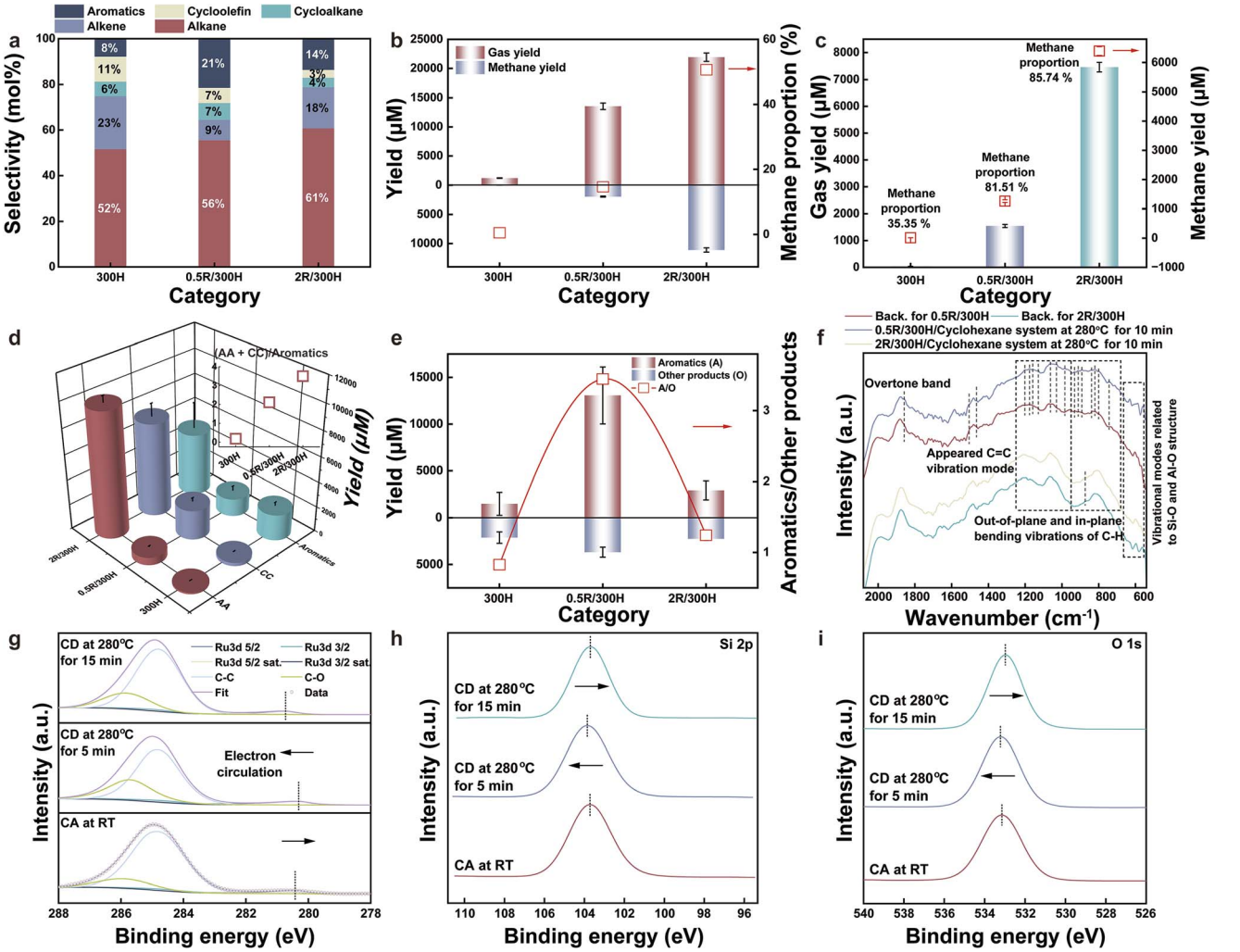

Fig. 3 A systematic examination of mechanisms in polymer upcycling *via* probing reactions. (a) Selectivity analysis of alkane, alkene, cycloalkane, cycloolefin, and aromatic products in *X*R/300H/*n*-hexadecane/H_2-free/solvent-free systems. (b) Gas product yield and methane proportion in *X*R/300H/*n*-hexadecane/H_2 systems. (c) The yield of gas product and methane proportion in *X*R/H/cyclohexane/H_2 systems. (d) Yield determination of alkane + alkene (AA) and cycloalkane + cycloalkene (CC) and the AA + CC to aromatics ratio in *X*R/300H/benzene/H_2 systems. (e) Yields of aromatics and other products with the aromatics to other products ratio in *X*R/300H/cyclohexane systems. (f) *In situ* DRIFTS analysis of 0.5R/300H/cyclohexane and 2R/300H/cyclohexane systems from 2080 to 540 cm^{-1}. High-resolution figures can be viewed in Fig. S45 and S47. *In situ* XPS analysis of the 0.5R/300H/cyclohexane system: (g) analysis of Ru 3d XPS spectra; (h) analysis of Si 2p XPS spectra; (i) analysis of O 1s XPS spectra. CA and CD indicate cyclohexane adsorption and cyclohexane dehydrogenation, respectively.

along with more H_2 consumption (*i.e.*, 25 532.06 μM *vs.* 32 965.01 μM for 0.5R/300H and 2R/300H, respectively, Fig. S37), suggesting that large Ru NPs may energetically favor C–C cleavage in comparison to Ru ACs, as low-index flat planes are typically required for alkane adsorption.[9] In addition, a greater amount of liquid hydrocarbons (*i.e.*, alkane, alkene, cycloalkane, and cycloalkene) was obtained in the 2R/300H/hexadecane/H_2 system compared to the 0.5R/300H/hexadecane/H_2 system (*i.e.*, 33 289.95 μM *vs.* 38 555.22 μM for 0.5R/300H and 2R/300H, respectively, Fig. S38). This also suggested that 2R/300H exhibited superior H_2 utilization capacity for C–C cleavage and recombination compared to 0.5R/300H. These results indicated that the 2R/300H favored the hydrogenolysis pathway more than the 0.5R/300H, which aligns with the phenomena observed in LDPE upcycling (*i.e.*, increased gas hydrocarbon yield upon increasing the metal loading, Fig. S33). Note that the chain extension was observed in both systems (*i.e.*, detected products with carbon numbers greater than 16, Fig. S39 and 40), which can be ascribed to the synergism between Ru metal (*i.e.*, cleavage of larger hydrocarbons into smaller fragments) and acidic sites (*i.e.*, chain extension enabled by recombination and rearrangement).

As the concentration of available surface hydrogen (H*) diminished, the possibility of the C chain undergoing further C–C bond cleavage prior to H*-assisted desorption increased.[25] Therefore, conditions that depleted adsorbed H* elevated selectivity towards C–C bond scission. H* exhibited stronger binding on step edges compared to terrace sites, implying that smaller Ru ACs, with a higher proportion of these defect sites, maintained greater steady-state H* coverage compared to Ru

NPs (Fig. 1j and k). This explained the observed lower selectivity towards gaseous short-chain hydrocarbons on smaller Ru ACs due to higher H* concentrations (*i.e.*, superior H* binding capacity on Ru ACs compared to Ru NPs, evidenced in Fig. 2i). Conversely, larger NPs, with more extensive terrace areas, were more likely to provide strong polymer adsorption but low H* binding capacity that was conducive to C–C bond cleavages (Fig. 4b), thereby resulting in high gas yield (Fig. 3b). Alternatively, this disparity can be ascribed to the elevated density of highly reactive under-coordinated Ru atoms (such as those at corners and edges) on smaller Ru particles, which exhibited less sensitivity to the challenge of cleaving the initial C–H bond compared to the more coordinated sites on the surfaces of larger particles.[25] From another perspective, the higher surface H* coverage in Ru ACs compared to Ru NPs may also promote the desorption of the dehydrogenated species of alkanes, indirectly affecting hydrogenolysis activity but maintaining an appropriate C=C formation rate.[9,26] Note that the increased availability of H* on Ru ACs can be attributed to two key factors: (i) a favorable binding affinity for H* and (ii) an enhanced yield of H* from the robust dehydrogenation reactions of cycloalkanes and cycloalkenes.

The regioselectivity for C–C cleavage was observed, generating more methane in the 2R/300H group compared to that in 0.5R/300H (1975.86 μM *vs.* 11 112.13 μM for 0.5R/300H and 2R/300H, respectively, Fig. 3b). This can also be ascribed to the H* binding differences between large and small Ru NPs. Typically, the higher *H coverage on low-loading Ru ACs favored internal C–C bond cleavage (*i.e.*, lower hydrogen liberation) over terminal C–C bond cleavage (higher hydrogen liberation). The

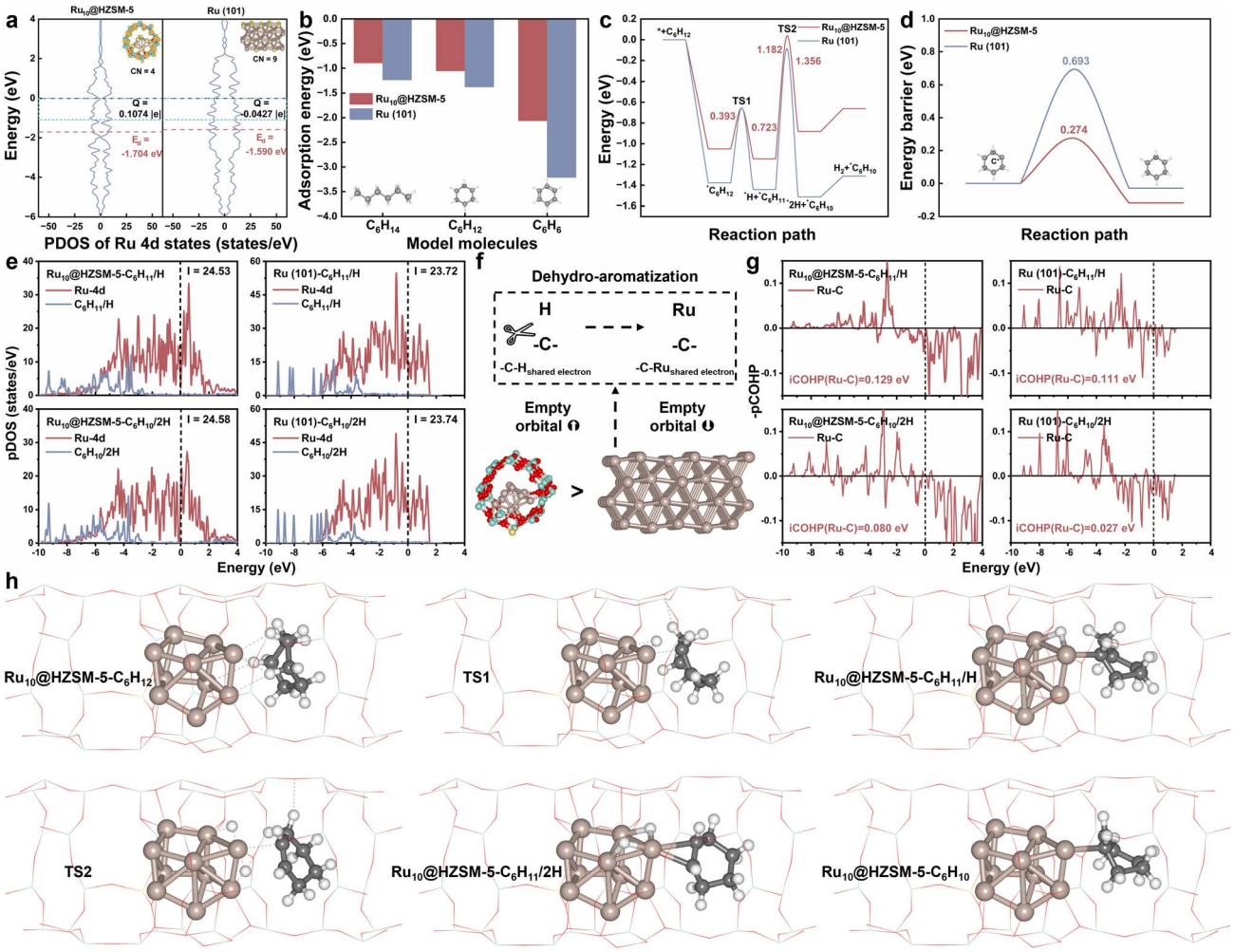

Fig. 4 A systematic examination of mechanisms in polymer upcycling *via* theoretical simulation. (a) The calculated DOS with the d band center, Bader charge, and CN of Ru in Ru_{10}@HZSM-5 and Ru (101) surfaces. (b) The calculated adsorption energy of C_6H_{14}, C_6H_{12}, and C_6H_6 on Ru_{10}@HZSM-5 and Ru (101) surfaces. (c) Energy profiles of the step-by-step dehydrogenation from C_6H_{12} to C_6H_{10} on Ru_{10}@HZSM-5 and Ru (101) surfaces. (d) The calculated hydrogen migration energy barrier from H* on active sites to C_6H_{11} with C^+ on Ru_{10}@HZSM-5 and Ru (101) surfaces. (e) The calculated DOS of Ru_{10}@HZSM-5 – C_6H_{11}/H, Ru_{10}@HZSM-5 – C_6H_{10}/2H, Ru (101) – C_6H_{11}/H, and Ru (101) – C_6H_{10}/2H. *I* represents the integration above the Fermi level. (f) The optimized structures of Ru_{10}@HZSM-5 and Ru (101) surfaces. Si: cyan; Ru: grey; Al: light yellow; O: red. (g) The calculated –*p*COHP of Ru–C bonds in Ru_{10}@HZSM-5 – C_6H_{11}/H, Ru_{10}@HZSM-5 – C_6H_{10}/2H, Ru (101) – C_6H_{11}/H and Ru (101) – C_6H_{10}/2H. (h) The optimized intermediate structures adsorbed on Ru_{10}@HZSM-5. Si: cyan; Ru: grey; Al: light yellow; O: red; C: black; H: white.

converse situation can be expected for larger Ru counterparts.[9] An enhanced CH_4 yield during LDPE upcycling was also observed with increased Ru loading, highlighting the improved C–C cleavage capacity and regioselectivity associated with higher Ru loading levels compared to lower loading levels (Fig. S33).

To sum up, as the surface complex became more progressively dehydrogenated in the alkane hydrogenolysis reaction, a greater number of free neighboring Ru atoms are needed to effectively accommodate the H*, rationalizing the conclusion that the low-index crystal face with continuous Ru atoms can more readily drive frequent alkane hydrogenolysis through dehydrogenative adsorption compared to Ru ACs without enough continuous isolated metal sites (*i.e.*, rapid desorption of intermediates that contain C=C due to high H* coverage-mediated adsorption inhibition).[27] Besides, identical results were observed in the hydrogenolysis reaction of cyclohexane, where a higher yield of gaseous products and enhanced proportion of methane were detected for the 2R/300H compared to 0.5R/300H (Fig. 3c). These results indicated that the 0.5R/300H can maintain the yield of aromatics by inhibiting the hydrogenolysis reaction in the polymer upcycling reaction.

The re-hydrogenation of the benzene ring can largely decrease the aromatics yield. For example, concurrent cyclohexane dehydrogenation and benzene hydrogenation by switching temperature were observed in a Pt(111) single crystal-mediated cyclohexane dehydrogenation reaction.[28] Therefore, the capacity of re-hydrogenation was determined over 0.5R/300H and 2R/300H using the benzene ring as a probe molecule. More hydrogenation products of the benzene ring (*i.e.*, cyclohexane + cycloalkene (C/C)-related products) and hydrogenolysis products of the benzene ring (*i.e.*, alkane + alkene (A/A)-related products) were observed in the 2R/300H/benzene/H_2 system (2372.42 and 610.11 μM for CC and AA, respectively, Fig. 3d) compared to that in the 0.5R/300H/benzene/H_2 system (7431.46 and 9934.31 μM for CC and AA, respectively, Fig. 3d). Concurrently, more H_2 consumption was observed for 2R/300H compared to 0.5R/300H (30 928.9322 μM *vs.* 19 201.9957 μM, Fig. S41). Effective co-adsorption of aromatic rings and H_2 is essential for catalyzing the hydrogenation of aromatic compounds.[29] Therefore, it is plausible that the limited surface area of Ru ACs impeded this co-adsorption. The elevated barrier for aromatic ring adsorption on Ru ACs, as opposed to flat surfaces possessed by Ru NPs (refer to 2.3.2), resulted in a decreased selectivity toward cyclohexane, cycloalkene, alkane, and alkene-related products in benzene hydrogenation and LPDE upcycling (Fig. 3d and 1b).

Similarly, more gas yield was observed for the 2R/300H/benzene/H_2 system (9435.059913 μM, Fig. S42) compared to the 0.5R/300H/benzene H_2 system (295.025733 μM, Fig. S42), which likely stemmed from the intensified competition for low-coordination sites between the hydrocarbon intermediate and H*, inhibiting subsequent C–C cleavage, as the smaller particles typically exhibit a more pronounced response to variations in H* coverage compared to larger counterparts.[25] More benzene alkylation products were observed in the 2R/300H compared to the 0.5R/300H-mediated benzene hydrogenation reaction (Fig. S43), which should be ascribed to the enhanced acidity-facilitated alkylation processes (Fig. S11 and 12).[30] It can be concluded that the 0.5R/300H, characterized by high H* coverage and a weaker co-adsorption capacity for H* and aromatics compared to 2R/300H, exhibited reduced C–C cleavage and re-hydrogenation capacity, thereby maintaining a high yield of aromatics.

Cyclohexane was selected as a model substrate to compare the dehydro-aromatization capacities of 0.5R/300H and 2R/300H. More aromatics yields (*i.e.*, 13 064.18 μM and 2926.54 μM for 0.5R/300H and 2R/300H, respectively, Fig. 3e) as well as larger aromatics/other products ratio (*i.e.*, 3.45 and 0.95 for 0.5R/300H and 2R/300H, respectively, Fig. 3e) were observed for 0.5R/300H compared to 2R/300H (Fig. 3e). Simultaneously, increased and dominant ring opening products (*i.e.*, hexane, 295.98 μM with a hexane proportion in total gas (HP) of 85.38% and 1600.74 μM with HP of 91.88% for 0.5R/300H and 2R/300H, respectively) were observed for 2R/300H compared to 0.5R/300H (Fig. S44). These results highlighted that the ring opening was more preferred over dehydrogenation in a large Ru NP-incorporating zeolite. Superior aromatics yield of Ru ACs can be thus associated with the following reasons: (i) intrinsically superior dehydrogenation capacity of Ru ACs compared to Ru NPs, (ii) inclined re-transformation of aromatics towards naphthene by hydrogenation and subsequent hydrogenolysis on large Ru NPs (Fig. 3d).

The turnover frequency (TOF) for aromatics production decreased with increased loading (*i.e.*, 544.34 μM mg_{Ru}^{-1} h^{-1} and 30.48 μM mg_{Ru}^{-1} h^{-1} for 0.5R/300H and 2R/300H, respectively), which may be attributed to the inaccessibility of a fraction of Ru, given that activities are normalized based on total Ru content. An alternative explanation for the declined TOF with higher Ru loading is that the dehydrogenation activity is intrinsically dependent on the structural characteristics of the Ru active sites. Also, it was demonstrated that enhanced redox activity can be expected for decreased particle domain size, which would facilitate C–H bond activation. Similarly, a maximum turnover frequency for Cu-loaded KIT-6 was observed at a Cu surface density of 0.047 Cu per nm^2, higher than that for 0.011 and 0.024 Cu per nm^2 and 0.097, 0.242, 0.421, and 0.694 Cu per nm^2.[31] In a separate sample, a low-coordinated W atom of WO_{3-x} donated electrons to C_6H_{12}, weakening its C–H bond, also highlighting the more effective efficacy of Ru ACs in activating the C–H bond of cyclohexane compared to Ru NPs.[32]

In situ DRIFTS was employed to further elucidate the role of particle attributes in the dehydrogenation reaction (Fig. 3f, S45, and S46). Peaks observed at approximately 2930 cm^{-1} (C–H asymmetric stretching vibration of methylene) and 2852 cm^{-1} (C–H symmetric stretching vibration of methylene) are attributed to the adsorption of cyclohexane. The peaks at 2319 and 2360 cm^{-1} can be ascribed to the adsorption of CO_2, which is difficult to eliminate completely. Notable C–H in-plane bending vibrations associated with substituted benzene (1250–1000 cm^{-1}), C–H out-of-plane bending vibrations related to substituted benzene (910–665 cm^{-1}), C=C stretching vibrations linked to substituted benzene (1600–1450 cm^{-1}) and overtone bands related to

substituted benzene (2000–1650 cm^{-1}) were observed in the 0.5R/300H/cyclohexane system, in contrast to the 2R/300H/cyclohexane system, which exhibited no significant signals. Furthermore, the stretching vibrations of the C–H group (3300–3100 cm^{-1}) indicated the formation of unsaturated carbons (Fig. S45 and S46), which were not clearly detected in the 2R/300H/cyclohexane system as well. Therefore, Ru ACs exhibit a greater propensity to drive the dehydrogenation reaction compared to Ru NPs, attributed to their superior hydrogen abstraction efficiency.

To summarize (Fig. 5), the observed superiority of 0.5R/300H over 2R/300H can be attributed to its enhanced dehydrogenation capacity, which effectively facilitated the rapid initiation of depolymerization through metal–acid synergism. Additionally, its effective cyclization capability promoted the formation of hexacarbon rings, while the rapid aromatization process enabled the generation of aromatic compounds. Simultaneously, the comparatively weaker re-hydrogenation and hydrogenolysis abilities of 0.5R/300H result in reduced side reactions, such as aromatic hydrogenation and excessive C–C cleavage, ultimately contributing to a higher yield of aromatics.

To elucidate the nature of the active site in 0.5R/300H during the cyclohexane dehydrogenation, *in situ* XPS was employed to monitor the valence state changes of Ru, O, and Si (Fig. 3g–i). Periodic electron gain and loss in Ru 3d (280.42 eV → 280.31 eV → 280.73 eV), corresponding to periodic electron loss and gain in Si 2p (103.72 eV → 103.85 eV → 103.70 eV)/O 1s (533.15 eV → 533.22 eV → 532.98 eV), were observed, underscoring the metal–support interaction that facilitated cyclohexane dehydrogenation. The electron exchange observed in Ru species highlighted its crucial role in cyclohexane adsorption, H

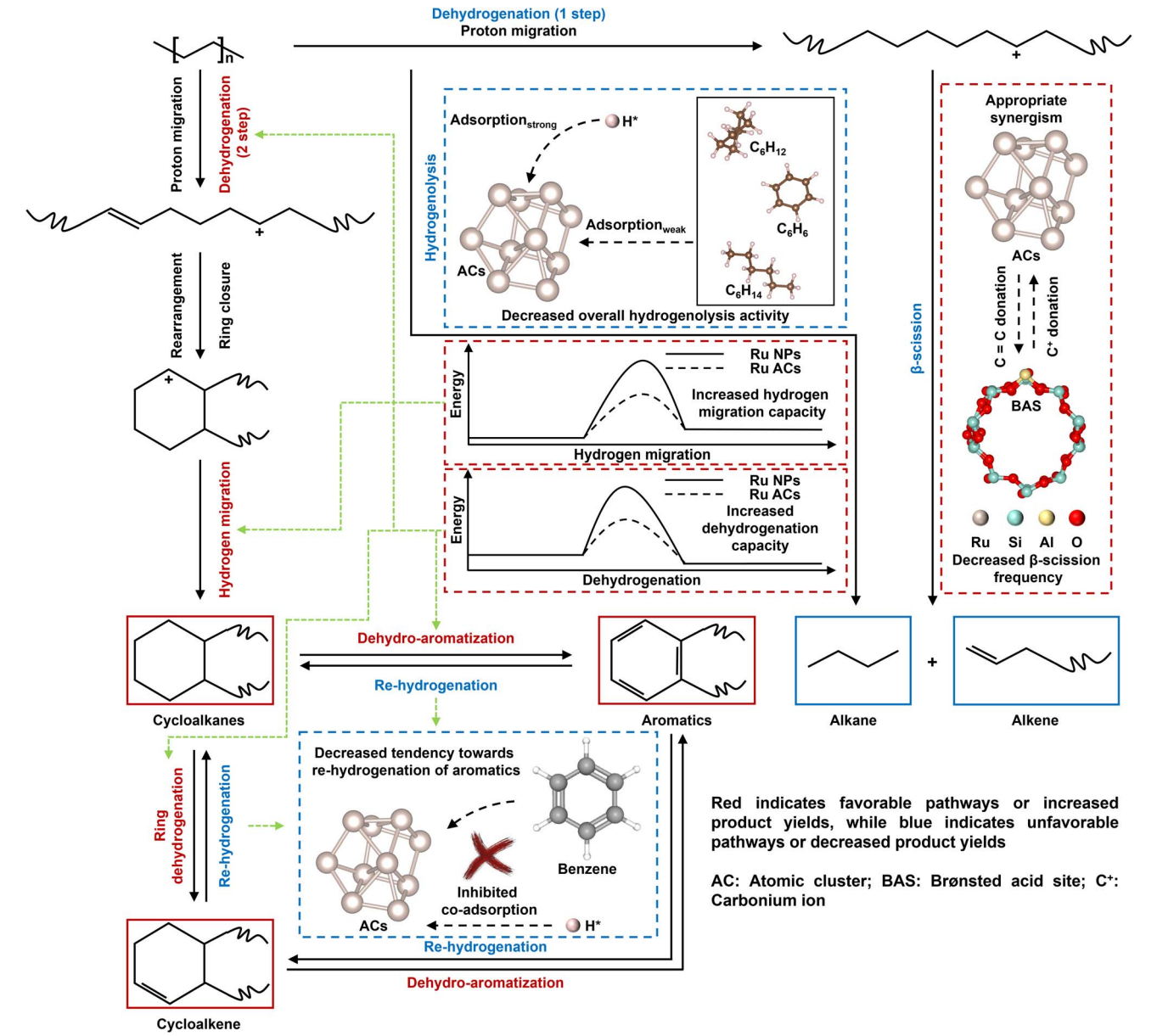

Fig. 5 The distinct edges of Ru AC-loaded HZSM-5 over Ru NP-loaded HZSM-5 in plastics upcycling.

generation, and product desorption. Additionally, Si_xAl_yO may function as an electron reservoir, accommodating the abstracted H to enable sequential dehydrogenation of adsorbed aromatics, followed by re-formation and release of H_2.

2.3.2 An in-depth exploration of the mechanisms involved in the polymer upcycling: theoretical simulation perspectives. The theoretical models for 0.5R/300H and 2R/300H were meticulously constructed to elucidate the advantages of Ru ACs over Ru NPs at both atomic and orbital levels. ZSM-5 was described by the periodic MFI framework (sourced from the Database of Zeolite Structures, **http://www.iza-structure.org/databases/**). Ru_{10}@HZSM-5 and Ru (101) were used to describe the Ru ACs with isolated Ru atoms and Ru NPs with a continuous lattice fringe, respectively (Fig. S48).

Atomic assemblies featuring abundant coordination-unsaturated sites, such as kinks, steps, and edges, typically exhibit superior catalytic performance due to their distinct electronic properties, characterized by the shifted d-band center. To be specific, the interaction atoms positioned in ACs and acting sites on the lattice plane possessed averaged Ru–Ru coordination numbers (CNs) of 4 and 9, respectively. Accordingly, their d-band centers varied from −1.704 eV to −1.590 eV (Fig. 4a and Table S6). These variations critically impacted the binding affinity of participants to ACs and NPs.[33] The adsorption energies of C_6H_{14}, C_6H_{12}, and C_6H_6 on the Ru (101) surface were significantly higher than those on Ru_{10}@HZSM-5 (Fig. 4b, S49–54, and Table S7), consistent with the phenomena observed in probing experiments (Fig. 3). Specifically, the increased adsorption energies of C_6H_{14} and C_6H_{12}, combined with a weak binding capacity for H* (Fig. 2i), contributed to an excessively strong C–C cleavage on the Ru (101) surface, thereby enhancing the yield of chain hydrocarbons. In addition, the excessively strong interaction with C_6H_6 may adversely promote coke formation and impede subsequent reaction cycles due to the coverage of active sites, ultimately leading to a diminished capacity for overall reaction efficiency especially cyclohexane dehydro-aromatization. Additionally, the strong adsorption of C_6H_6 would also enhance the potential for re-hydrogenation. These results underscored the pivotal role of surface structural characteristics in optimizing catalytic performance.

The differences in the electronic structures between Ru AC and Ru NP models should be responsible for the varied interaction intensity as well. The calculated average Bader charges of Ru were $0.1074|e|$ and $-0.0427|e|$ for Ru_{10}@HZSM-5 and Ru (101), respectively (Fig. 4a and Table S8). These results indicated that Ru on the Ru (101) surface possessed a higher electronic density compared to Ru_{10}@HZSM-5, particularly with enhanced electron density positioned between −1 and 0 eV (Fig. 4a). This increased electronic density facilitated a more effective interaction with the lowest unoccupied molecular orbital (LUMO) of C_6H_x, resulting in greater adsorption energy.[34]

In the LDPE dehydrogenation reaction, the superiority of isolated Ru sites compared to crystallographic plane Ru sites can be reflected in the following aspects:

① Ru_{10}@HZSM-5 exhibited a significantly reduced dehydrogenation energy barrier during hexane dehydrogenation (*i.e.*, simulating LDPE dehydrogenation) compared to Ru (101), decreasing from 1.552 eV to 0.568 eV, thereby demonstrating its superior LDPE activation and dehydrogenation capacity (Fig. S48b and c(1–3)).

② The greater energy decline (0.3913 eV and 0.1105 for Ru_{10}@HZSM-5 and Ru (101), respectively) during TS desorption further enhanced the rapid reaction cycle (*i.e.*, adsorption–desorption circulation) during initiating the LDPE depolymerization (Fig. S48b and d(1–3)).

The core model reaction of aromatics formation (*i.e.*, cyclohexane dehydrogenation with the liberation of one H_2 molecule) was investigated. The Ru (101) surface was excessively active toward cyclohexane adsorption with an adsorption energy of −1.38 eV (Fig. 4c and Table S9) compared to Ru_{10}@HZSM-5 with an adsorption energy of −1.05 eV (Fig. 4c and Table S10), potentially resulting in a higher energy barrier for subsequent reaction steps.[35] In detail, high adsorption energy in catalysis will significantly impact subsequent product transformations by strengthening the stability of adsorbed reactants. This strong interaction often increases the activation energy for transition states, slows reaction rates, and can lead to catalyst deactivation through mechanisms such as catalyst poisoning (*i.e.*, coke formation due to weak product desorption, Fig. S20). Additionally, the high adsorption energy may restrict conformational changes in the reactants and introduce kinetic barriers, ultimately affecting the overall thermodynamic and kinetic feasibility of the reaction pathway. For example, although the Pd (111) can activate the scission of the first two C–H bonds in dodecahydro-*N*-ethylcarbazole (DNEC) as efficiently as Pd_{13}/G in kinetic aspects, the thermodynamically sluggish product desorption step enabled weak dehydrogenation performance of Pd (111).[21]

Correspondingly, both C–H activation and C–H cleavage steps were less thermodynamically favorable on Ru (101) compared to Ru_{10}@HZSM-5, with energy barriers of 0.393 eV *vs.* 0.723 eV for the first C–H bond cleavage and 1.182 eV *vs.* 1.356 eV for the second C–H bond cleavage (Fig. 4c). Note that the strong van der Waals interactions contributed to a calculated adsorption energy of C_6H_6 on Ru (101) of −3.213 eV, which was significantly higher than that on Ru_{10}@HZSM-5 (−2.062 eV). This indicated that the surface sites on Ru (101) were more prone to poisoning by C_6H_6, thereby obstructing further activation of C_6H_{12} (Fig. 4b).

These results were in accordance with the TGA, showing that more aromatics were formed in the (2R/300H + cyclohexane) system relative to the (0.5R/300H + cyclohexane) system, highlighting that lattice fringe catalysis is also confronted with the inferior product desorption capacity, easily enabling coke formation and activity decline (Fig. S22). The strong adsorption capacity of Ru NPs with the lattice fringe compared to isolated Ru ACs for reactants and products can be ascribed to the greater distribution of d-band electrons around the Fermi energy level (Bader charge of $-0.0427|e|$ *vs.* $0.1074|e|$, Fig. 4a and Table S8), which was closely associated with the more positive d-band center (−1.590 eV *vs.* −1.704 eV, Table S6).

The migration of H* to eliminate carbonium ions represents a crucial step in the formation of dehydro-aromatization precursor-hexatomic carbon rings-related products. Therefore,

the capability of Ru assemblies to facilitate hydrogen migration and to eliminate or stabilize carbenium ions was evaluated. Notably, a significantly higher migration energy barrier of 0.693 eV was observed for Ru (101), in contrast to the migration energy barrier of merely 0.274 eV for Ru_{10}@HZSM-5 (Fig. 4d and Table S11). These findings underscored that Ru (101) may lack the requisite activity to effectively facilitate the production of cyclic hydrocarbons, thereby resulting in a sluggish overall reaction dynamics.

The detailed density of states (DOS) and integrated crystal orbital Hamilton population (ICOHP) analyses were employed to investigate the differences in the activity for dehydroaromatization between Ru ACs and Ru NPs, with a focus on the intermediates C_6H_{11} + H and C_6H_{10} + 2H. On the one hand, the Ru_{10}@HZSM-5 demonstrated a greater presence of vacant orbitals (*i.e.*, integration above the Fermi level) compared to Ru (101) following the dehydrogenation of C_6H_{12} (resulting in C_6H_{11} + H) and C_6H_{11} (resulting in C_6H_{10} + H). This enhanced availability of empty orbitals promoted a more favorable reaction pathway for subsequent hydrogen abstraction processes (*i.e.*, the transfer of shared electrons in C–H to that in Ru–C) (Fig. 4e). This result can be further validated by the more intense pCOHP distribution (*i.e.*, indicating reaction participation) for Ru_{10}@HZSM-5 compared to Ru (101) above the Fermi level (Fig. 4g). On the other hand, electronic exchange was more readily observed in Ru_{10}@HZSM-5 compared to Ru (101). This phenomenon was primarily due to the increased ICOHP value of the Ru–C bond—rising from 0.111 eV to 0.129 eV for C_6H_{11} + H and from 0.027 eV to 0.080 eV for C_6H_{10} + 2H (Fig. 4g). Additionally, the bonding proportion with the d orbital was optimized (Fig. S55 and Table S12): for C_6H_{11} + H, it shifted from 35.65% (with d_{xy} dominance for Ru_{10}@HZSM-5) to 31.41% (with d_{z^2} dominance for Ru (101)); for C_6H_{10} + 2H, it changed from 30.67%/10.70% (with $d_{xz}/d_{x^2-y^2}$ dominance for Ru_{10}@HZSM-5) to 17.81%/16.54% (with d_{z^2}/d_{yz} dominance for Ru (101)). This excessive bonding with the d_{z^2} orbital may compromise bonding stability due to its potential electronic interactions with the antibonding orbitals of C_6H_x.[36]

It is evident that C_6H_x actively interacted with the step, kink, and edge sites—referred to as low-coordination sites—within Ru ACs, in stark contrast to Ru NPs, which predominantly featured high-coordination sites (Fig. 4h and S56). Note that the higher density of step sites associated positively with the enhanced reaction activity. To comprehend this experimental finding, Nørskov *et al.*[11] and Nakai *et al.* examined the dependence of mass-specific activity and the ratio of step sites on the size of hexagonally close-packed (hcp) Ru NPs constructed according to the Wulff theorem at the nanoscale. Step sites were observed in NPs larger than 2 nm, peaking in density at approximately 2.5 nm before declining noticeably with further increases in particle size. The B5 site, pivotal in Ru-based catalysts for ammonia synthesis, predominantly resides at step sites. The modulation of step-site density due to varying particle size correlates well with computed activity levels.[37] This underscored the critical role of particle size in optimizing ensemble density on metal catalysts to enhance catalytic performance. To sum up (Fig. 5), the pronounced superiority of Ru ACs relative to Ru NPs can be partially ascribed to the excessively high adsorption energy associated with Ru NPs. This phenomenon not only restricted the efficient circulation of subsequent reaction pathways but also facilitated re-hydrogenation, hydrogenolysis, and the formation of coke. Moreover, the elevated energy barriers for dehydrogenation and hydrogen migration further diminished the overall catalytic performance of Ru NPs in comparison to Ru ACs.

2.4 Strategic optimization of support acidity and comprehensive investigation of practical application efficacy

The acidity intensity was adjusted by varying the Si/Al ratio from 300 to 150 and 75. On the one hand, optimum metal–acid synergism was achieved with 0.5R/150H, facilitating the generation of a greater amount of liquid hydrocarbons (Fig. 6a–c and S57). Note that the drop in conversion rate and aromatics selectivity for 0.5R/75H should be ascribed to coke formation (*e.g.*, excessive fusion of benzene) and occurrence of side reactions (*e.g.*, high acidity-facilitated C–C over-cracking through β-scission), which can be verified by the increased mass loss at 380–650 °C in thermogravimetric analysis (TGA) and enhanced alkane/alkene proportion in products (Fig. S58 and 6c), respectively.[30,38] The decreased aromatics-related H ratio in ^{1}H NMR spectra supported the occurrence of various side reactions as well (Fig. S59 and S60).

On the other hand, the superiority of isolated ACs compared to NPs with an intact lattice plane was further verified (Fig. 6a–c), extending the applicability of the principle to various acidities. It can be concluded that Ru ACs exhibited superior dehydrogenation capability, and their synergistic effect with BAS enhanced the efficiency of ring formation while suppressing the β-scission predominantly driven by BAS and bypassing the hydrogenolysis and re-hydrogenation promoted by large Ru NPs, leading to a reduced yield of chain hydrocarbons and enhanced LDPE conversion rate (Fig. 6a–c). The RDS (with different dehydrogenation barriers among different H positions) may vary among the Ru-loaded 300H, 150H, and 75H supports (*i.e.*, with changing cycloalkane to cycloolefin ratio between pure support, 0.5 wt%, and 2 wt% over different supports), however, overall showing enhanced total hydrocarbon and aromatics yield at 0.5 wt% Ru incorporation compared to 2 wt% Ru incorporation (Fig. 6b and c).

TGA revealed that 0.5R/300H produced significantly less coke than 2R/300H (Fig. S20), indicating that Ru ACs have enhanced resistance to coking due to their unique structural properties that limit the adsorption and polymerization of reaction intermediates (*i.e.*, decreased residual time). Additionally, the 0.5R/150H catalyst exhibited the lowest coke production and highest catalytic activity among the tested samples (0.5R/75H and 0.5R/300H). This improved performance was attributed to an optimal metal–acid balance, which maintained sufficient acidity to facilitate intermediate conversion while minimizing coke formation. In contrast, 0.5R/75H, despite lower coke production than 0.5R/300H, did not achieve the same optimal balance, as its higher acidity could lead to increased polymerization of intermediates and excessive β-

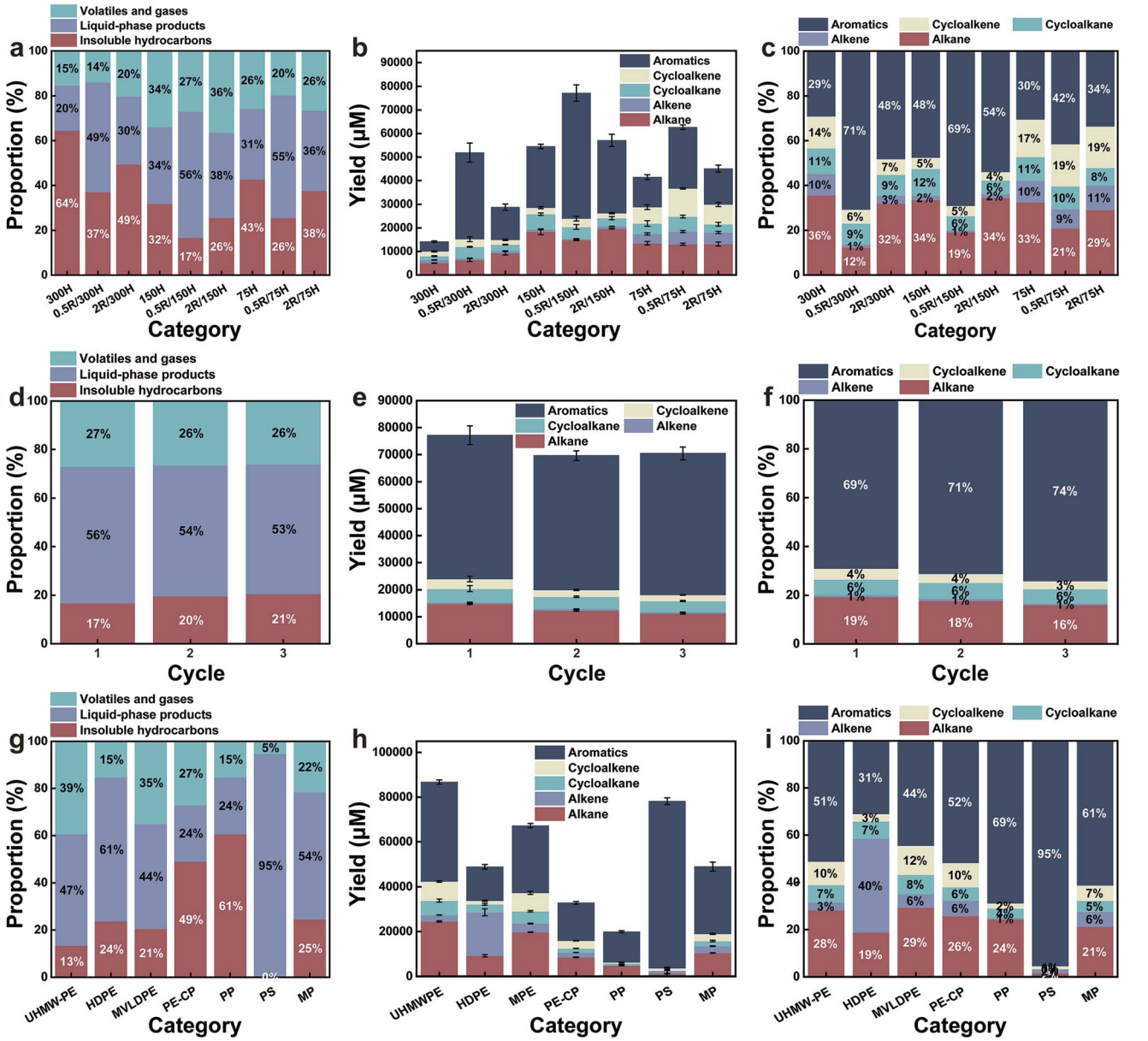

Fig. 6 Strategic enhancement of support acidity and in-depth analysis of practical application efficacy. (a) Selectivity of volatiles/gases, liquid-phase products, and insoluble hydrocarbons, (b) molar quantities of products, (c) selectivity of alkanes, alkenes, cycloalkanes, cycloolefins, and aromatic products in *X*R/*Y*H/LDPE/H_2-free/solvent-free systems ($X = 0$, 0.5, 2; $Y = 300$, 150, 75). (d) Selectivity of volatiles/gases, liquid-phase products, and insoluble hydrocarbons, (e) molar quantities of products, (f) selectivity of alkanes, alkenes, cycloalkanes, cycloolefins, and aromatic products in sequential experimental runs. (g) Selectivity of alkanes, alkenes, cycloalkanes, cycloolefins, and aromatic products, (h) molar quantities of products, (i) selectivity of alkanes, alkenes, cycloalkanes, cycloolefins, and aromatic products in common plastics upcycling reactions.

scission (*i.e.*, maximized alkane/alkene yield, Fig. 6b and c; coke deposition, Fig. S58; coal detection, Fig. S61 and S62). Overall, these findings highlight the superior anti-coking properties of Ru ACs compared to NPs and the importance of optimizing acid density for enhanced catalytic efficiency.

To investigate the practical application potential of the 0.5R/150H in plastics upcycling, a series of consecutive reactions following the regeneration of the spent 0.5R/150H were conducted. The results revealed that both the conversion rates and product distributions remained virtually unchanged (Fig. 6d–f), underscoring the stability in the solvent- and hydrogen-free upcycling of LDPE. Also, they highlighted that the coke can be easily removed through combustion, effectively restoring it to the original upcycling capacity. Moreover, the spent 0.5R/150H displayed stable AC morphology and size distribution, suggesting the stability of active sites (Fig. S63).[39]

Furthermore, the 0.5R/150H demonstrated exceptional performance in the upcycling of a diverse range of plastics, including ultra-high-molecular-weight PE (UHMWPE), high-density PE (HDPE), metallocene PE (MPE), PE dipping powder

(PEDP), polystyrene (PS), polypropylene (PP), and blended plastics (UHMW-PE : HDPE : MVLDPE : PP : PS = 1 : 1 : 1 : 1 : 1). The observed conversion rates and aromatics selectivity for these polymers were 86.64/51%, 76.26/31%, 79.49/44%, 50.9/52%, 39.42/69%, 99.94/95%, and 75.5/61%, respectively (Fig. 6g–i). These results highlighted the remarkable robustness of 0.5R/150H as a practical thermos-catalytic upcycling catalyst, effectively addressing polymers with different densities, branching degrees, and typical processing contaminants. A significant amount of polycyclic aromatic hydrocarbons (PAHs) derived from the upcycling of polystyrene (PS) was observed, including compounds such as naphthalene, 2-phenyl- [612-94-2], naphthalene, 2-methyl- [91-57-6], and anthracene, 9-ethenyl- [2444-68-0]. These PAHs were generated through the fusion of dissociated benzene substrates. Despite their high toxicity, PAHs can be utilized in applications such as dyes/pigments, plastic additives, and lubricating oils.

3 Conclusion

This study elucidated the transformative potential of hydrogen- and solvent-free thermal upcycling of plastic waste through the innovative use of Ru AC-loaded HZSM-5. The results demonstrated that Ru ACs significantly outperformed traditional Ru NP-loaded HZSM-5 in both conversion rates (*i.e.*, 62.93 *vs.* 51.66%), selectivity for valuable aromatics (*i.e.*, 70.43 *vs.* 43.65%), and TOF (*i.e.*, 52.71 *vs.* 10.63 $mg_{LDPE}\ mg_{Ru}^{-1}\ h^{-1}$), offering compelling economic advantages (*i.e.*, economic profit *vs.* economic loss).

In detail, the atomic assembly structure of Ru ACs led to overall optimal intermediate adsorption energies, enhanced dehydrogenation and dehydro-aromatization capacities, a decreased H* migration energy barrier, alleviated tendency towards re-hydrogenation of aromatics and continuous C–C cleavage, *etc.*, which collectively streamlined reaction dynamics. From the atomic and orbital levels, the increased availability of empty orbitals in Ru ACs and reduced participation of the d_{z^2} orbital contributed to the optimal Ru–C interaction during the dehydro-aromatization reaction. Consequently, the TOF for aromatics production from cyclohexane dehydro-aromatization increased from 30.48 μM $mg_{Ru}^{-1}\ h^{-1}$ for 2R/300H to 544.34 μM $mg_{Ru}^{-1}\ h^{-1}$ for 0.5R/300H, respectively.

Additionally, the theoretical scalability of this approach, applicable to various metals, supports, and acidities, underscored the broader implications of these findings. By systematically optimizing the metal–acid balance, the LDPE conversion rate increased from 62.93% to 87% and the capability for effective upcycling of a wide range of common plastics was achieved.

This comprehensive exploration not only highlighted the superiority of ACs over NPs in waste plastic upcycling but also provided valuable mechanistic insights that can be leveraged for the design of more effective and cost-efficient catalysts. Ultimately, these advancements contribute significantly to the sustainability of polymer recycling processes, aligning with global efforts toward sustainable development and environmental stewardship. Future research should focus on the practical implementation of these findings to further enhance the feasibility and efficiency of plastic waste upcycling technologies.

4 Materials and methods

Detailed materials and methods can be found in the SI, including chemicals and materials, catalyst preparation, characterization, experimental and analytical methods, and theoretical calculations.

Author contributions

Fan Mo: investigation, conceptualization, methodology, validation, writing – original draft, writing – review & editing. Qixing Zhou: funding acquisition, project administration, supervision, writing – review & editing. Pengfei Wang: methodology. Weitao Liu: methodology. Chuan Yin: methodology. Zelin Hou: methodology. Wendan Xue: methodology. Qi Wang: methodology. Jianling Wang: methodology. Tong Zheng: methodology. Zongxin Tao: methodology. Xiang Li: methodology.

Conflicts of interest

The authors declare that there are no conflicts of interest related to this research. No financial or personal relationships have influenced the work presented in this paper.

Data availability

The data supporting the findings of this study are available within the main article and its SI.

The supplementary information file contains additional data and detailed methodologies that support the findings of this study. See DOI: **https://doi.org/10.1039/d5sc04662a**.

Acknowledgements

This work was financially supported by the Ministry of Science and Technology of the People's Republic of China as a key Research & Development program project (grant no. 2023YFC3709001), the National Natural Science Foundation of China (NSFC) as a NSFC-BRICS project (grant no. 32461143206), and the Tianjin Science and Technology Bureau as a key science and technology supporting project (grant no. 19YFZCSF00920). The authors would like to thank Shiyanjia Lab (**https://www.shiyanjia.com/**), SCI-GO (**https://www.sci-go.com**), and eceshi (**https://www.eceshi.com/**) for helping with experimental analyses, and the Applied Chemistry and Engineering Institute (Nankai University) for the instrument support of ACTEM (JEM-ARM200F).

References

1 F. Zhang, M. Zeng, R. D. Yappert, J. Sun, Y.-H. Lee, A. M. LaPointe, B. Peters, M. M. Abu-Omar and S. L. Scott,

Polyethylene upcycling to long-chain alkylaromatics by tandem hydrogenolysis/aromatization, *Science*, 2020, **370**, 437–441.

2 UNEP, *World Environment Day brings solutions to plastic pollution into focus*.

3 H. Ran, S. Zhang, W. Ni and Y. Jing, Precise activation of C–C bonds for recycling and upcycling of plastics, *Chem. Sci.*, 2024, **15**, 795–831.

4 W. Zimmermann, Biocatalytic recycling of plastics: facts and fiction, *Chem. Sci.*, 2025, **16**, 6573–6582.

5 J. Du, L. Zeng, T. Yan, C. Wang, M. Wang, L. Luo, W. Wu, Z. Peng, H. Li and J. Zeng, Efficient solvent- and hydrogen-free upcycling of high-density polyethylene into separable cyclic hydrocarbons, *Nat. Nanotechnol.*, 2023, **18**, 772–779.

6 S. Kim, C. Park and J. Lee, Reduction of polycyclic compounds and biphenyls generated by pyrolysis of industrial plastic waste by using supported metal catalysts: A case study of polyethylene terephthalate treatment, *J. Hazard. Mater.*, 2020, **392**, 122464.

7 Q. Kang, M. Chu, P. Xu, X. Wang, S. Wang, M. Cao, O. Ivasenko, T. K. Sham, Q. Zhang, Q. Sun and J. Chen, Entropy confinement promotes hydrogenolysis activity for polyethylene upcycling, *Angew. Chem., Int. Ed.*, 2023, **62**, e2023131.

8 W. Tu, M. Chu, X. Wang, X. Wang, Y. Li, W. Yang, M. Cao, L. Wang, Y. Li, T.-K. Sham, Y. Cui, Q. Zhang and J. Chen, SMSI-induced charge transfer for selective hydrogenolysis of polyolefins, *Appl. Catal., B*, 2023, **339**, 123122.

9 L. Chen, L. C. Meyer, L. Kovarik, D. Meira, X. I. Pereira-Hernandez, H. Shi, K. Khivantsev, O. Y. Gutiérrez and J. Szanyi, Disordered, sub-nanometer Ru structures on CeO_2 are highly efficient and selective catalysts in polymer upcycling by hydrogenolysis, *ACS Catal.*, 2022, **12**, 4618–4627.

10 L. R. Karadaghi, E. M. Williamson, A. T. To, A. P. Forsberg, K. D. Crans, C. L. Perkins, S. C. Hayden, N. J. LiBretto, F. G. Baddour, D. A. Ruddy, N. Malmstadt, S. E. Habas and R. L. Brutchey, Multivariate bayesian optimization of CoO nanoparticles for CO_2 hydrogenation catalysis, *J. Am. Chem. Soc.*, 2024, **146**, 14246–14259.

11 K. Honkala, A. Hellman, I. N. Remediakis, A. Logadottir, A. Carlsson, S. Dahl, C. H. Christensen and J. K. Nørskov, Ammonia synthesis from first-principles calculations, *Science*, 2005, **307**, 555–558.

12 J. P. den Breejen, P. B. Radstake, G. L. Bezemer, J. H. Bitter, V. Frøseth, A. Holmen and K. P. de Jong, On the origin of the cobalt particle size effects in Fischer–Tropsch catalysis, *J. Am. Chem. Soc.*, 2009, **131**, 7197–7203.

13 M. A. Newton, A. J. Knorpp, V. L. Sushkevich, D. Palagin and J. A. van Bokhoven, Active sites and mechanisms in the direct conversion of methane to methanol using Cu in zeolitic hosts: A critical examination, *Chem. Soc. Rev.*, 2020, **49**, 1449–1486.

14 J. S. Woertink, P. J. Smeets, M. H. Groothaert, M. A. Vance, B. F. Sels, R. A. Schoonheydt and E. I. Solomon, A $[Cu_2O]^{2+}$ core in Cu-ZSM-5, the active site in the oxidation of methane to methanol, *Proc. Natl. Acad. Sci. U. S. A.*, 2009, **106**, 18908–18913.

15 A. Masson, B. Bellamy, Y. H. Romdhane, M. Che, H. Roulet and G. Dufour, Intrinsic size effect of platinum particles supported on plasma-grown amorphous alumina in the hydrogenation of ethylene, *Surf. Sci.*, 1986, **173**, 479–497.

16 Z. Cen, X. Han, L. Lin, S. Yang, W. Han, W. Wen, W. Yuan, M. Dong, Z. Ma, F. Li, Y. Ke, J. Dong, J. Zhang, S. Liu, J. Li, Q. Li, N. Wu, J. Xiang, H. Wu, L. Cai, Y. Hou, Y. Cheng, L. L. Daemen, A. J. Ramirez-Cuesta, P. Ferrer, D. C. Grinter, G. Held, Y. Liu and B. Han, Upcycling of polyethylene to gasoline through a self-supplied hydrogen strategy in a layered self-pillared zeolite, *Nat. Chem.*, 2024, **16**, 871–880.

17 X. Chen, M. Peng, D. Xiao, H. Liu and D. Ma, Fully exposed metal clusters: Fabrication and application in alkane dehydrogenation, *ACS Catal.*, 2022, **12**, 12720–12743.

18 L. Zhang, M. Zhou, A. Wang and T. Zhang, Selective hydrogenation over supported metal catalysts: From nanoparticles to single atoms, *Chem. Rev.*, 2020, **120**, 683–733.

19 Y. Yuan, E. Huang, S. Hwang, P. Liu and J. G. Chen, Confining platinum clusters in indium-modified ZSM-5 zeolite to promote propane dehydrogenation, *Nat. Commun.*, 2024, **15**, 6529.

20 G. Celik, R. M. Kennedy, R. A. Hackler, M. Ferrandon, A. Tennakoon, S. Patnaik, A. M. LaPointe, S. C. Ammal, A. Heyden, F. A. Perras, M. Pruski, S. L. Scott, K. R. Poeppelmeier, A. D. Sadow and M. Delferro, Upcycling single-use polyethylene into high-quality liquid products, *ACS Cent. Sci.*, 2019, **5**, 1795–1803.

21 C. Dong, Z. Gao, Y. Li, M. Peng, M. Wang, Y. Xu, C. Li, M. Xu, Y. Deng, X. Qin, F. Huang, X. Wei, Y.-G. Wang, H. Liu, W. Zhou and D. Ma, Fully exposed palladium cluster catalysts enable hydrogen production from nitrogen heterocycles, *Nat. Catal.*, 2022, **5**, 485–493.

22 Z. Hou, F. Mo, Q. Zhou, Y. Xie, X. Liu, T. Zheng and Z. Tao, Key role of vegetation cover in alleviating microplastic-enhanced carbon emissions, *Environ. Sci. Technol.*, 2024, **58**, 3288–3301.

23 B. Whajah, N. da Silva Moura, J. Blanchard, S. Wicker, K. Gandar, J. A. Dorman and K. M. Dooley, Catalytic depolymerization of waste polyolefins by induction heating: Selective alkane/alkene production, *Ind. Eng. Chem. Res.*, 2021, **60**, 15141–15150.

24 L. Li, J. Cai, Y. Liu, J. Ni, B. Lin, X. Wang, C.-t. Au and L. Jiang, Zeolite-seed-directed Ru nanoparticles highly resistant against sintering for efficient nitrogen activation to ammonia, *Sci. Bull.*, 2020, **65**, 1085–1093.

25 H. Shi, X. Li, G. L. Haller, O. Y. Gutiérrez and J. A. Lercher, Active sites and reactive intermediates in the hydrogenolytic cleavage of C–C bonds in cyclohexane over supported iridium, *J. Catal.*, 2012, **295**, 133–145.

26 H. Shi, O. Y. Gutiérrez, G. L. Haller, D. Mei, R. Rousseau and J. A. Lercher, Structure sensitivity of hydrogenolytic cleavage of endocyclic and exocyclic C–C bonds in methylcyclohexane over supported iridium particles, *J. Catal.*, 2013, **297**, 70–78.

27 B. Coq and F. Figueras, Structure–activity relationships in catalysis by metals: some aspects of particle size, bimetallic and supports effects, *Coord. Chem. Rev.*, 1998, **178–180**, 1753–1783.
28 B. Wang and G. F. Froment, Dehydrogenation of cyclohexane on Pt(111) in a bulb reactor, *Catal. Lett.*, 2017, **147**, 663–673.
29 Y. Jing, Y. Wang, S. Furukawa, J. Xia, C. Sun, M. J. Hülsey, H. Wang, Y. Guo, X. Liu and N. Yan, Towards the circular economy: Converting aromatic plastic waste back to arenes over a Ru/Nb_2O_5 catalyst, *Angew. Chem., Int. Ed.*, 2021, **60**, 5527–5535.
30 J. Wei, R. Yao, Q. Ge, D. Xu, C. Fang, J. Zhang, H. Xu and J. Sun, Precisely regulating Brønsted acid sites to promote the synthesis of light aromatics *via* CO_2 hydrogenation, *Appl. Catal., B*, 2021, **283**, 119648.
31 S. L. Nauert, A. S. Rosen, H. Kim, R. Q. Snurr, P. C. Stair and J. M. Notestein, Evidence for copper dimers in low-loaded CuO_x/SiO_2 catalysts for cyclohexane oxidative dehydrogenation, *ACS Catal.*, 2018, **8**, 9775–9789.
32 F. Quan, G. Zhan, X. Liu, B. Zhou, H. Gu, L. Yu, L. Yang, F. Jia, X. Liu and L. Zhang, Photocatalytic oxidative dehydrogenation of cyclohexane to cyclohexene over oxygen-deficient tungsten trioxide, *Appl. Catal., B*, 2021, **298**, 120549.
33 A. Nilsson, L. G. M. Pettersson and J. K. Nørskov, *Chemical Bonding at Surfaces and Interfaces*, 2008.
34 Y. Deng, Y. Guo, Z. Jia, J.-C. Liu, J. Guo, X. Cai, C. Dong, M. Wang, C. Li, J. Diao, Z. Jiang, J. Xie, N. Wang, H. Xiao, B. Xu, H. Zhang, H. Liu, J. Li and D. Ma, Few-atom Pt ensembles enable efficient catalytic cyclohexane dehydrogenation for hydrogen production, *J. Am. Chem. Soc.*, 2022, **144**, 3535–3542.
35 F. Mo, C. Song, Q. Zhou, W. Xue, S. Ouyang, Q. Wang, Z. Hou, S. Wang and J. Wang, The optimized Fenton-like activity of Fe single-atom sites by Fe atomic clusters-mediated electronic configuration modulation, *Proc. Natl. Acad. Sci. U. S. A.*, 2023, **120**, e2300281120.
36 S. Pan, X. Yang, J. Sun, X. Wang, J. Zhu and Y. Fu, Competitive adsorption mechanism of defect-induced d-orbital single electrons in $SrRuO_3$ for alkaline hydrogen evolution reaction, *Adv. Energy Mater.*, 2023, **13**, 2301779.
37 A. Ishikawa, T. Doi and H. Nakai, Catalytic performance of Ru, Os, and Rh nanoparticles for ammonia synthesis: A density functional theory analysis, *J. Catal.*, 2018, **357**, 213–222.
38 S. Singh, J. Martínez-Ortigosa, N. Ortuño, V. Polshettiwar and J. García-Martínez, Enhanced efficiency in plastic waste upcycling: the role of mesoporosity and acidity in zeolites, *Chem. Sci.*, 2024, **15**, 20240–20250.
39 W. Xue, Q. Zhou, P. Wang, S. Zuo, F. Li, J. Jiang, F. Mo, C. Yin, G. Liu, Z. Ban, Y. Wei, W. An, X. Huang, H. Wang and S. Zhan, Sulfur-mediated transformation from osmium nanocrystals to single atoms for efficient alkaline hydrogen evolution reaction, *Proc. Natl. Acad. Sci. U. S. A.*, 2025, **122**(27), e2426207122.